Flame intensity analysis for hot molten metal pouring in the steel industry by applying image segmentation

Ivan Popov and Grazia Todeschini

Swansea University, College of Engineering, Fabian Way, Swansea, SA1 8EP

708967@swansea.ac.uk; grazia.todeschini@swansea.ac.uk

Abstract: Pouring large quantities of hot metal (HM) can release substantial amounts of flame. This problem is frequently encountered within the Basis Oxygen Furnace (BOF) steelmaking process where large quantities of HM (frequently exceeding 300 t) are poured into the converter vessels. The HM is contained in specially designed ladles and poured using overhead girder cranes. Excess release of flame may damage surrounding components such as crane ropes and consequently reduce their lifecycle. Therefore, limiting the release of flame during pouring, allows extending the lifetime of the components located in proximity of the ladle. The scope of this paper is to characterise flame generation during different pouring operations at a BOF steelmaking plant and to relate the amount of flame generated to process factors. Due to the complexity of the process under investigation, this paper does not aim to eliminate flame generation, but rather to identify approaches to its mitigation. The proposed approach utilises a standard CCTV camera to record videos of pours. An image segmentation analysis is then performed, where the flame is separated from the background image using pixel information in the CIE L*a*b* colour space. For each frame, flame intensity is then calculated. This process is partially automated for each video making use of MATLAB. A total of 169 videos are analysed and the pours that cause higher flame intensity are identified. In the last steps of the analysis, the process factors with the most significant impact on the flame release are identified and mitigating solutions are proposed.

Keywords: flame intensity analysis, image segmentation, process control, steel industry, lifecycle management.

1. Introduction

In a Basic Oxygen Furnace (BOF) a mixture of hot liquid iron and steel scrap is turned into steel through a process where oxygen is blown into the molten metal at supersonic speeds, removing carbon from the melt through oxidation. The BOF process involves three main stages: charging, blowing and tapping. During charging phase, the scrap and the hot liquid iron are loaded into the converter vessel. In the blowing stage, fluxes are added to aid the oxidation process and a water-cooled lance, through which oxygen is supplied, is inserted into the vessel and oxygen blowing is initiated. The last stage involves tapping of the converter vessel, to allow liquid steel to exit through a tapping nozzle, separating molten steel from carbon heavy slag.

Scrap amount, varying between 15 and 25% of the total metal weight in the converter vessel, are loaded during the charging phase and vary by size and composition depending on the grade of steel being manufactured [1]. Charging with hot metal (HM) then takes place where hot iron is poured into the converter vessel from hot metal ladles. In modern Basic Oxygen Steelmaking (BOS) plants, the ladles have a capacity to hold over 300 t of HM. Specialised overhead girder charging cranes are used to transport the full hot metal ladles and pour their contents in to the converter vessel. Heat, in the form of flame, is released during pouring, reaching temperatures of 1300^{o} C, and causing thermal damage to the crane and surrounding structures [2]. To minimise damage to these components, the release of flame during HM charging needs to be minimised. The flame intensity and propagation vary with each consecutive charge and depends on several process factors. A diagram of flame release during HM pouring into a BOF converter vessel is displayed in Figure 1, where the main components involved in the process are shown: the ladle, the converter vessel and the hooks used to lift and tilt the ladle.

The above concerns are well-known in the steelmaking industry and several research groups have studied this process. The heat front from HM pouring into a converter vessel was previously recorded in [3] using infrared imaging. The aim of this work was to analyse the thermal damage caused to charging crane cables and to develop a cable condition monitoring system.

Along with flames, metallic fumes and dusts are released while pouring the HM. In [4], several video recordings were used to analyse the amount of fumes released during charging. The average fume flow rate and

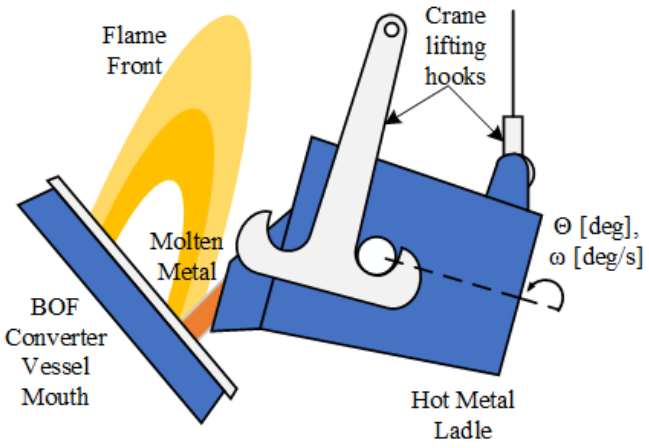

Figure 1. Diagram of HM pouring into BOF converter vessel.

total mass were then evaluated and used in a Computational Fluid Dynamic (CFD) model. Similarly in [5], CFD simulations were carried out based on analysis performed by recording emissions releases during HM pouring. The following data was used as an input to the model: flame temperature, recorded using a thermocouple device positioned in the vicinity of the flame front, gas concentration and flow velocity. For a separate model, the volume of smoke plume released was determined using structural particle image velocimetry.

The use of flame segmentation has been applied in other industrial processes, specifically those in relation to the metal manufacturing industries. In [6], the flame from an iron ore sintering furnace was segmented by first pre-treating images containing furnace flame using Discrete Fourier transformation and then by applying Red Green Blue (RGB) colour space decomposition. Examples of processing flame images in rotary sintering kilns can be found in [7] and [8], providing designs for complex flame recognition systems. A system for recognising flame regions in a Blast Furnace raceway for the estimation of temperature using pixel colour information is presented in [9].

Flame segmentation has also been applied to study the behaviour of flame in industrial boilers. In [10], a flame segmentation algorithm for use with infrared images is presented, where the shape of the flame is divided into multiple geometries. A Bayesian approach is used to estimate the boundary regions of each geometry. This segmentation algorithm was tested on a flame generated by a boiler burner and characterised against process conditions. An algorithm based on visible light spectrum images has also been developed for this application [11]. This boiler flame segmentation is based on YCbCr colour space with automatic thresholding of luma (Y) and chroma (Cr) components.

According to the literature review carried out, no previous studies have been performed where image segmentation was used to analyse flame produced during HM charging. In this paper, a method of analysing the causes of high flame release is proposed. The approach consists in performing a colour segmentation analysis on video recordings of HM pouring into a converter vessel to estimate the intensity of the produced flame. Flame intensity is then related to process factors. A case study was performed at the Tata Steel Port Talbot BOS plant, where a CCTV camera (Pelco Sarix Enhanced IME322 [12]) was positioned in proximity to the converter mouth to record the HM charging operation. Using MATLAB, each video was transformed into CIE L*a*b* colour space and a segmentation algorithm was applied to calculate flame intensity. An evaluation was then made against known process conditions. The results from this case study, where 169 pouring videos were analysed, are presented in this paper.

2. CIE L*a*b* colour space.

The majority of commercially available video acquisition devices, including the CCTV camera used for this project, output video in an RGB format. For each pixel, this method encodes a value ranging from 0-255 for the individual R (red), G (green) and B (blue) colour component. Although colour segmentation in images is possible using the RGB format, in this paper the CIE L*a*b* colour space was utilised since it is more uniform than other colour spaces, allowing for better colour representation of the flame [13].

The CIE L*a*b* colour space consists of 3 components: L* - Luminance (or lightness) , which ranges from 0 (black) to 100 (white), a* - ranging from -128 (green) to 128 (red), and b* - ranging from -128 (blue) and 128 (yellow). As a result, the CIE L*a*b* colour space provides a spherical 3D representation of the colour spectrum,

where each individual colour has its own cartesian coordinate [14]. This is displayed in Figure 2. Colour space conversion from RGB to CIE L*a*b* can be done using the following equations [15]:

$$\begin{bmatrix} X \\ Y \\ Z \end{bmatrix} = [M] \begin{bmatrix} R \\ G \\ B \end{bmatrix} \tag{1}$$

$$L^* = \begin{cases} 116 \times \sqrt[3]{Y/Y_r} - 16, & \text{for } (Y/Y_r) > 0.008856, \\ 903.3 \times (Y/Y_r), & \text{otherwise,} \end{cases} \tag{2}$$

$$a^* = 500 \times \left(f(X/X_r) - f(X/X_r)\right), \tag{3}$$

$$b^* = 200 \times \left(f(Y/Y_r) - f(Z/Z_r)\right), \tag{4}$$

$$f(t) = \begin{cases} \sqrt[3]{t}, & \text{for } t > 0.008856, \\ 7.787 \times t + 16/116 & \text{otherwise,} \end{cases}$$

Where $[M]$ is the RGB to XYZ conversion matrix (in this case $[M]$ is the conversion matrix for standard RGB (sRGB) [16]), R, G and B are the data channels from RGB encoding ranging from 0-255 and X_r , Y_r and Z_r are reference values of colour white (in this case taken as 0.9504, 1.0000 and 1.0888 respectively [17]).

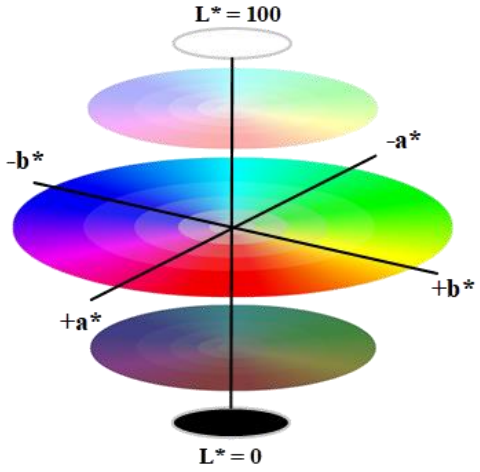

Figure 2. CIE L*a*b* 3D coordinate representation.

3. Nearest Neighbour Colour Segmentation

Image segmentation based on the analysis of colour spectrum, falls under two categories: supervised and unsupervised. In supervised classification, the segmentation region classifiers are typically pre-identified by the user. In unsupervised classification, these regions are estimated using the spectral colour information of a given image [18]. Although requiring prior knowledge to establish classifiers by the user, the use of supervised classification may lead to higher accuracy image segmentation results [19].

In the videos recorded for this work, colour variation was caused only by the appearance of flame. Since the camera was placed in a fixed location, and an indoor environment, variations due to ambient conditions were excluded. Due to the lack of external factors influencing colour variation, a supervised classification method was chosen as it was deemed possible to determine the classification parameters using a single example video.

The Nearest Neighbour (NN) algorithm [20, 21] was used in this analysis due to its simple implementation and accurate results [19, 22]. The NN algorithm works by evaluating a distance metric between a point of interest x and classifiers $y = \{y_1, y_2, y_3, \dots y_n\}$, where the smallest distance indicates the classification of x. When applied in colour-based image segmentation, points of interest are the individual pixels and the classifiers are colours to undergo segmentation. The distance calculation is performed on the colour space encoding values. Typically, the Euclidean distance metric is applied to find the minimum distance according to the following expression:

$$d(a,b) = \sqrt{\sum_{i=1}^{n} (a_i - b_i)^2} \tag{5}$$

where $d(a,b)$ is the calculated distance, a and b are the cartesian coordinates of x and y respectively and n is the dimensionality of x and y.

In this analysis, the CIE L*a*b* colour space was utilised for the classification of pixels and the distance metric $d(a,b)$ for each pixel was calculated using the L*, a* and b* encoding values [23]. Therefore, the dimensionality value n in (5) was set to 3 where the difference of a_i and b_i was calculated as the difference between the values of L*, a* and b* for pixel x and classifier y, respectively.

For this analysis, four classifiers were selected, and their corresponding L*, a* and b* values were determined from a single video recording of a HM charge. These four colours were further sub-classified as the primary colours of the flame and the secondary colours of the background image. The primary colours were white, and a yellow shade taken as a cumulative average from sampling the recorded flame images at different points. The secondary colours are brown and grey: the first used for the identification of background with flame reflection and the second without reflection. The L*, a* and b* values corresponding to the four classifiers are displayed in Table 1.

Table 1. L*, a* and b* classifiers

	L* (b_1)	a* (b_2)	b*(b_3)	Colour
y_1 - White	99	0	0	
y_2 - Yellow	90	-8	39	
y_3 - Brown	70	0	30	
y_4 - Grey	70	0	0	

4. Methodology

Image segmentation was performed using MATLAB ver. R2018a with Image Processing Toolbox [24] and Parallel Computing Toolbox [25]. The analysis was performed on each frame of the recorded videos: for example, with the recording set at 30 fps (frames per second), a 2:00 minute recording resulted in the analysis of 3600 frames. To reduce the computational time, a region of interest (ROI) was selected: each frame was cropped to display only the region where the flame is most prominent, resulting in an analysis window measuring 670x1100 pixels. Each pixel in this window was then transformed from RGB to the CEI L*a*b* colour space. The NN classification was then performed on each pixel using classifiers displayed in Table 1 and subsequently the image of flame was segmented from the background image. The last step in this analysis was the estimation of flame intensity, which was taken as the total count of the segmented pixels displaying flame. The flow diagram for the analysis of a single frame is displayed in Figure 3.

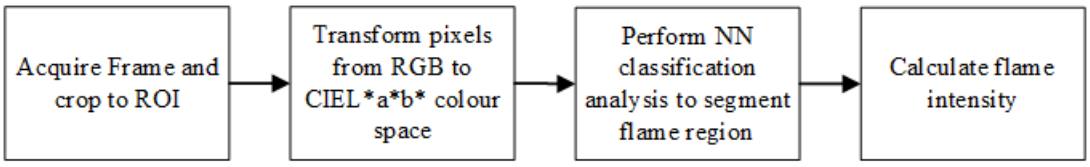

Figure 3. NN Flame segmentation flow chart

The analysis was repeated for each frame. The flame intensity for the entire video was taken as the average value of calculated flame intensity for the individual frames. Figure 4a displays a frame prior to the application of flame segmentation and Figure 4b displays the identical frame with the flame segmented from the background. For this image, the flame intensity was 37754. The overall average flame intensity for 169 recorded videos ranged from 7626 (Low flame) and 101523 (High flame).

5. Analysis of Results

In this section the results obtained from flame segmentation are compared against process factors. Pouring rate and scrap use are the two factors investigated in this work as main contributors to the production of flame. Other factors that may impact the amount of flame generated are not considered in this paper, although they may be taken into the account in future works.

At first, the relationships between 1. flame intensity and pouring rate and 2. flame intensity and total amount of scrap used are presented. Then, the contribution of different types of scrap to flame generation is assessed. Lastly, further analysis is carried out to determine the combination of pouring rate and scrap types to flame

(a) **(b)**

Figure 4. Example of flame segmentation: (a) original image and (b) after flame segmentation is applied.

generation. This section is concluded by providing suggestions on modifications of the pouring process to reduce flame intensity.

5.1. Average Pouring Rate and Flame Intensity

The first factor considered for the impact on flame intensity was average pouring rate. This parameter was determined by dividing the HM weight (ranging between 275 and 315 t) by the total pouring time. The total pouring time was calculated from the video recordings of each individual pour. The average pouring rate for the videos considered varied between 1.79 and 5.43 t/s. The actual rate differs at different stages of a pour due to the geometry of the ladle and individual pouring behaviours of the crane drivers. Figure 5 displays a scattered graph where pouring rate is plotted against the average flame intensity for each recording.

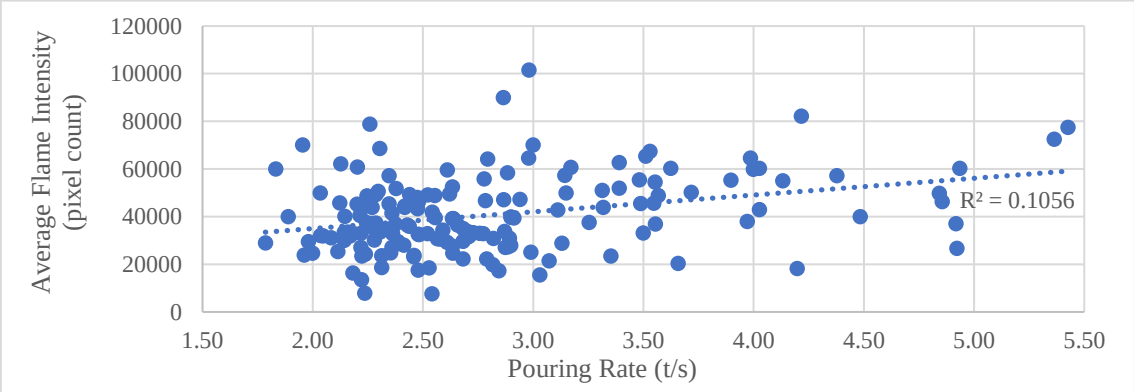

Figure 5. Plot showing Pouring Rate vs Average Flame Intensity

With the application of a trend line, a linear relationship is identified, suggesting that flame intensity increases with the increases in pouring rate. However, more insights are provided when the coefficient of determination (R^2) is calculated: this parameter is a statistical measure of how close the data is to the fitted regression line [26]. In theory, the value of R^2 ranges between 0 and 1, where values close to 1 signify that the regression line provides a good description of the data. For the case in Figure 5, the R^2 value is close to 0.11, indicating substantial scattering of the results. Therefore, a relationship between pouring rate and flame intensity could not be concluded based on this graph alone. This result suggests that there are other factors contributing to the generation of flame.

5.2. Scrap Amount and Flame Intensity

A comparison between scrap amounts and the average flame intensities is carried out in Figure 6. Similarly, to the previous graph a trend line was interpolated. The slope of the line in this case too suggests that flame intensity increases with the increase of scrap weight. However, the R^2 value in this case is close to 0.06: this

number is even lower than the one obtained in Figure 5 and indicates that scrap weight alone is not the only contributing factor in flame generation. Eight pours where no scrap was used were discarded from the results in Figure 6.

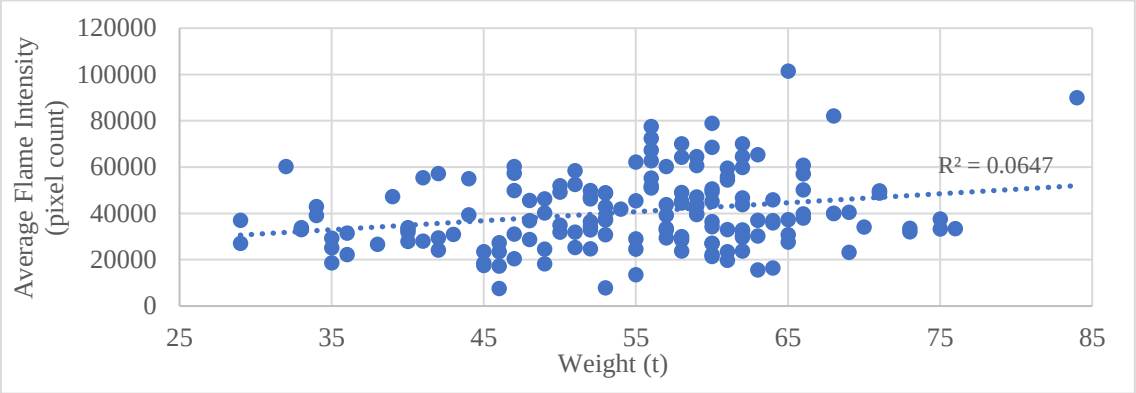

Figure 6. Plot showing Scrap wight vs Average flame intensity

5.3. Scrap Type – Frequency of Occurrence Analysis

At the Port Talbot BOS plant scrap is classified in to 9 groups: Turnings, A Steel Skull, C Steel Skull, Cold Iron, Tin/Steel Cans, Incinerated Bales, Mill Products/Slabs, Tundish Skull and A0/Demo. These scrap types can be further sub-categorised into internally (A and C Steel Skulls, Cold Iron, Mill Products/Slabs and Tundish Skull) and externally (Turning, Tin/Steel Cans, Incinerated Bales and AO/Demo) sourced scrap types [1]. Internal scrap arises from leftover solidified iron and steel and trimmings of steel strips/slabs. External scrap incorporates a variety of old commercial and industrial equipment, incinerator scrap and used tin coated steel cans [1]. Each scrap type varies in size and composition and its use depends on the grade of steel being manufactured. Internally sourced scrap is typically quite homogenous in its composition. Compositional variations are more prominent with externally sourced scrap types, varying in iron and impurity contents from batch to batch.

A further analysis was carried out to identify a pattern between the use of different scrap types and the generated flame intensity. In this analysis, the top and bottom quartile of pours with the highest and lowest recorded flame intensity, respectively, were considered. Excluding the pours where no scrap was used, a total of 40 pours were included in each top and bottom quartile. Each scrap type was further categorised into Low amount and High amount. These two categories were determined by taking the midpoint value between the maximum and minimum amounts recorded for each individual scrap type, where the values above the midpoint categorised as High and values equal to or below as Low. The maximum, minimum and midpoint weights for each scrap type are displayed in Table 2.

Table 2. Maximum, minimum and classification High/Low Limit value of scrap weight

Scrap Type	Max (t)	Min (t)	Midpoint (t)
Turnings	13	1	7
A Steel Skull	16	1	9
C Steel Skull	13	1	7
Cold Iron	25	3	14
Tin/Steel Cans	17	1	9
Incinerated Bales	15	2	9
Mill Products/Slabs	39	2	21
Tundish Skull	23	4	14
A0/Demo	3	2	2

The frequency of occurrence of each scrap type was determined for the pours included in the top and bottom quartiles using the Low and High scrap weight classifiers. Figure 7 shows the results for Low scrap: the frequency of occurrence is plotted for each scrap type. Two bars are shown: the orange corresponding to the top quartile and the blue to the bottom quartile. The frequency of occurrence appears to be uniform, with a maximum difference observed for Incinerated Bales and Mill products/Slabs. Figure 8 shows the same results for the case of High

scrap: in this case, the frequency of occurrence varies more visibly, where the uses of High A Steel Skull, C Steel Skull, Cold Iron, Tin/Steel Cans and Incinerated Bales are more frequent in the Top quartile. The uses of High Mill products/Slabs and Tundish Skull are more frequent in the Bottom quartile.

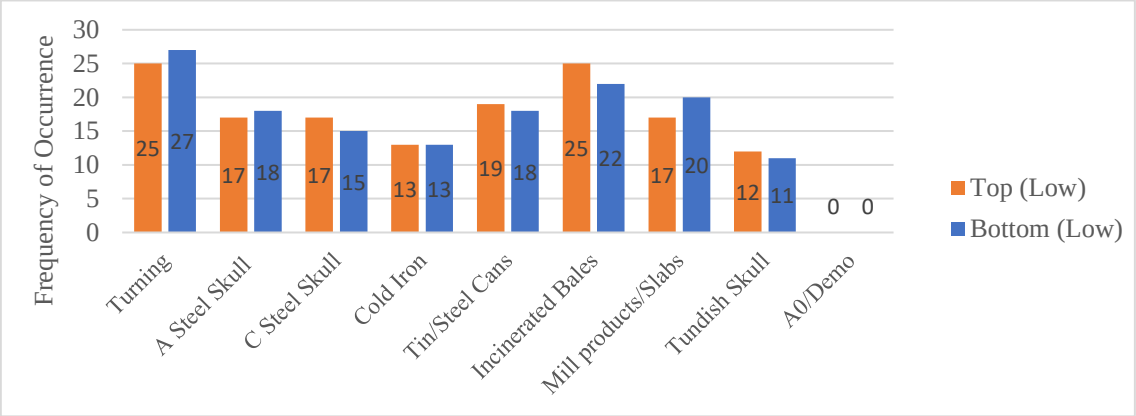

Figure 7. Bar chart of Top vs Bottom quartiles – Low scrap weight frequency

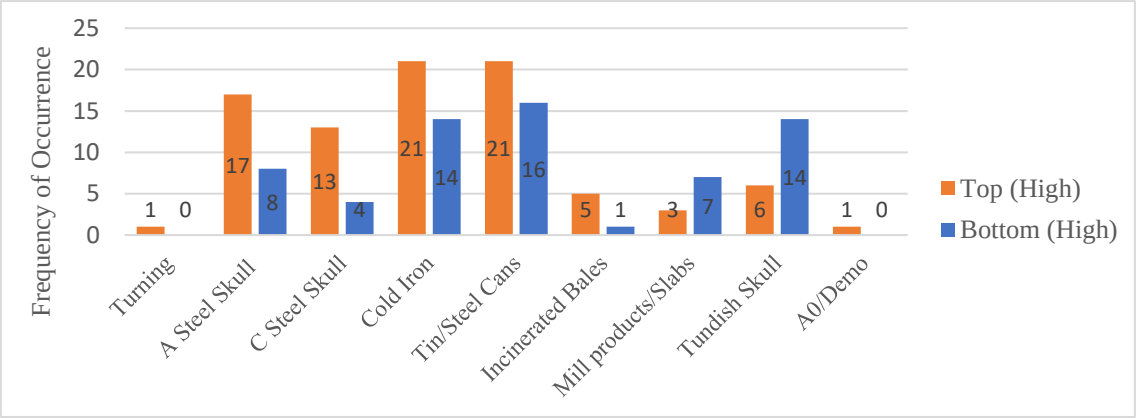

Figure 8. Bar chart of Top vs Bottom quartiles – High scrap weight frequency.

These results suggest that individual scrap types, when used in small amounts, have little to no influence on the intensity of generated flame. For high scrap amounts, a possible correlation between certain scrap types and flame intensity could be established, since A Steel Skull, C Steel Skull, Cold Iron, Tin/Steel Cans and Incinerated Bales are used in the highest amount in the top quartile. In turn, this suggests that the use of these scrap types, in high amounts, contributes to the production of flame.

5.4. Pouring Rate and Scrap Classification – High amount, high frequency scrap

In this section, the results from scrap classification and individual scrap type frequency use are analysed against pouring rates. The results from section 5.3 showed that there is a potential correlation between the use of high amounts of A Steel Skull, C Steel Skull, Cold Iron, Tin/Steel Cans and Incinerated Bales and high flame generation. The weights of the above mentioned five scrap types were summed for each pour, for the pours where their value was above the midpoint limit value (displayed in Table 2). Five groups were then identified, arranged by increasing value of the sum. These groups were: <10 t, 10-19 t, 20-29 t, 30-39 t and >39 t. The frequency of occurrence for each weight group were: 28, 53, 36, 19 and 26, respectively. Charges with no scrap were not considered in this analysis. Figure 9 displays the average value of flame intensities in each weight group. An increase of average flame intensity with increase of scrap amounts is observed, further indicating a correlation between the use of these scrap types and the generation of flame.

For each identified scrap weight group, the relationship between pouring rates and flame intensity is visualised via scatter graphs in Figures 10 (<10 t and 10-19 t), Figure 11 (20-29 t and 30-39 t) and Figure 12 (>39 t). By interpolating a trend line, a linear relationship between pouring rate and flame intensity is established and for each scrap group an increase in flame generation is expected with faster pouring rates. Referring to the R^2 value for

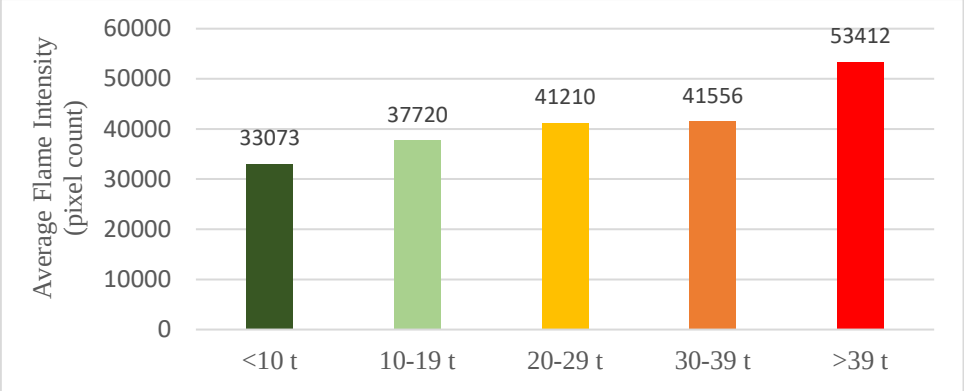

Figure 9. Bar chart of High freq. scrap weight groups vs average flame intensity

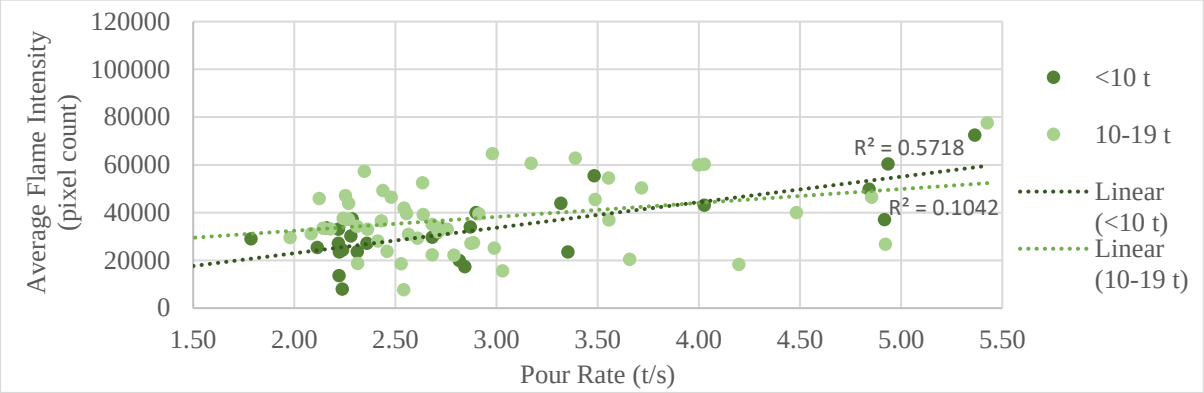

Figure 10. Plot showing pouring rate vs average flame intensity by High freq. weight, <10 t and 10-19 t.

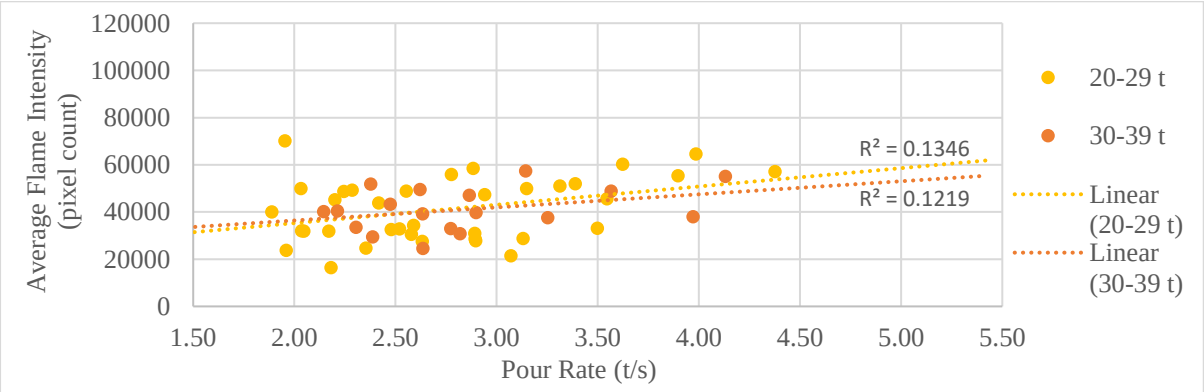

Figure 11. Pouring rate vs average flame intensity by High freq. weight, 20-29 t and 30-39 t.

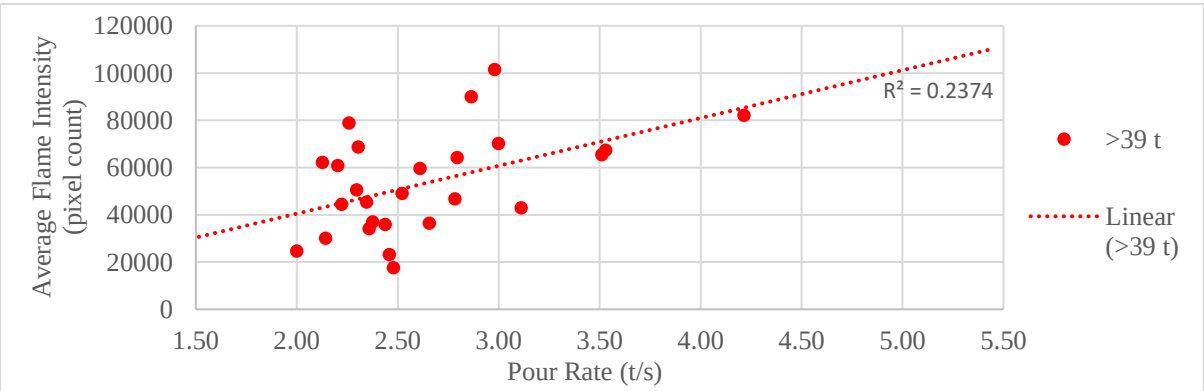

Figure 12. Pouring rate vs average flame intensity by High freq. weight, >39 t.

each scrap group, the best result is displayed for group <10 t, where R^2 is calculated to be 0.57. This value is deemed as acceptable in industrial process analysis, where human factors should be considered. In this context, the value is high enough to allow predicting the amount of flame generated with pouring rate to an acceptable level of accuracy. For groups 10-19 t, 20-29 t, 30-39 t and >39 t, the R^2 value is much lower, approximately measuring 0.1, 0.13, 0.12 and 0.24, respectively. This can also be shown by the increased scattering of points in these weight groups. This result can be explained by two factors: the pouring process is determined by the approach of individual crane drivers and the number of videos analysed is relatively small. It is expected that the analysis of more videos will provide further insights into the process factors.

5.5. Suggestions on Process Improvement

Based on the results obtained in this paper, suggestions can be made to improve the pouring process with the aim of reducing the amount of flame generated.

Firstly, from the results in Figure 9, by reducing the amount of scrap types that were identified to be major contributors to flame generation it is possible to reduce the generation of flame. However, this might not be a financially viable option since different scrap types have different costs and substituting them with scrap identified to have a lower impact could increase manufacturing costs. Additionally, the type of scrap used for each pour depends on the grade of steel being manufactured.

Secondly, it may be possible to reduce the generation of flame by adjusting the pouring rates in accordance to scrap weight groups and to the trend lines in Figures 10-12. For example, to keep the intensity of flame below an arbitrary value of 40000, for group <10 t, the pouring should be below 3.5 t/s and for 30-39 t pouring rate should be kept below approximately 2.5 t/s.

6. Conclusion

In this paper an analysis was carried out to correlate process factors to the generation of flame during charging of a converter vessel with HM. The two process factors considered in this work were the pouring rate and the use of metal scrap in the converter vessel. Image segmentation techniques were applied to 169 videos recording HM charging, in order to establish the average flame intensity for each pour. Regression analysis was then applied to find a correlation between the process factors described above and flame intensity. It was established that fast pouring and high amounts of total scrap contributed to the generation of flame. However, it was difficult to establish a linear relationship due to high spreading of results using these two factors alone.

By looking at the frequency of occurrence of individual scrap types in the bottom and top quartiles, arranged by their flame intensity, scrap types that have a major contribution to the generation of flame were established. Then, using the weight information of the identified high frequency scrap types, a refined relationship between the use of scrap, the pouring rate and the recorded flame intensity was established.

Through this analysis, possible process improvement suggestions were identified: specifically, using lower amounts of identified scrap and pouring liquid metal at a lower rate. Although it was difficult to establish a defined linear relationship between pouring rate, scrap weight and flame intensity, these results can be used as a basis for further analysis, to establish other process factors contributing to the generation of flame.

Acknowledgments

The authors would like to acknowledge the M2A funding from the European Social Fund via the Welsh Government (c80816) and Tata Steel UK that has made this research possible. Additionally, the authors would like to thank John Madill, Alison Tuling and Ben Jenkins of Tata Steel UK.

References:

[1] Short J., Grosvenor R.I., Prickett P.W. The development of a process charge expert system for a Basic Oxygen Steelmaking plant. 18th International Conference on Knowledge-Based and Intelligent Information & Engineering Systems; 15-17 September; Gdynia, Poland 2014.

[2] Popov V., Gabtykaev D. Cables with a steel core for hot-metal charging cranes. Metallurgist. 2008;52(9-10):588-591.

[3] Maslov V. Vlijanie termociklicheskih vozdejstvij rasplavlennogo metalla na sistemu "konverter-kran" i sovershenstvovanie ee jelementov [Influence of thermocyclic actions of molten metal on the "converter - crane" system and improvements of its elements]: Cherepovets State University; 2004.

[4] Plikas T., Woloshyn J., Johnson D. Application of CFD Modeling to the Design of Fume Control Systems in the Steel Industry. AIST Proceedings: AISTech 2007. 2007;1:745-756.

[5] Marx K., Roedl S. Efficient optimization of steel plant dedusting. Stahl und Eisen. 2012;132(5): [Pages Unknown].
[6] Chen W., Fubin W., Xianzhong C., Qingwen H., Zhikun C., Meng Z., et al. RGB color decomposition and image feature extraction of flame image in rear of sintering machine. 2017 36th Chinese Control Conference (CCC): IEEE; 2017. p. 5460-5463.
[7] Li W., Mao K., Chai T., Zhang H., Wang H. Gabor filter and eigen-flame image-based burning state recognition for sintering process of rotary kiln. 2011 50th IEEE Conference on Decision and Control and European Control Conference: IEEE; 2011. p. 3216-3221.
[8] Wang Q., Sheng Y., Chai L. Local entropy based pre-processing for flame images of alumina rotary kiln. 2014 9th IEEE Conference on Industrial Electronics and Applications: IEEE; 2014. p. 1476-1480.
[9] Zhang R., Cheng Y., Li Y., Zhou D., Cheng S. Image-based flame detection and combustion analysis for blast furnace raceway. IEEE Transactions on Instrumentation and Measurement. 2019;68(4):1120-1131.
[10] Marques J.S., Jorge P.M. Visual inspection of a combustion process in a thermoelectric plant. Signal processing. 2000;80(8):1577-1589.
[11] Xie M., Wu J., Zhang L., Li C. A novel boiler flame image segmentation and tracking algorithm based on YCbCr color space. 2009 International Conference on Information and Automation: IEEE; 2009. p. 138-143.
[12] Pelco. Saric IME Indoor and Environmental Mini Domes. Product Specification. [Location Unknown]; 2019 Apr 4.
[13] Celik T. Fast and efficient method for fire detection using image processing. ETRI journal. 2010;32(6):881-890.
[14] Sappi Fine Paper North America. Defining and Communicating Color: The CIELAB System. 2013. Available from: https://www.sappi.com/files/defining-and-communicating-colorpdf.
[15] Justin L.B. Useful Color Equations [Internet]. [Location Unknown]: Bruce Justin Lindbloom; [Date Unknown] [updated 2013 Jul 15; cited 2020 Apr 22]. Available from: http://www.brucelindbloom.com/index.html?Equations.html.
[16] Justin L.B. RGB/XYZ Matrices [Location Unknown]: Bruce Justin Lindbloom; [updated 2017 Apr 07; cited 2020 Apr 22]. Available from: http://www.brucelindbloom.com/index.html?Eqn_RGB_XYZ_Matrix.html.
[17] MathWorks. rgb2lab [Internet]. Natick, MA: The MathWorks; [Date Unknown] [cited 2020 April 22nd]. Available from: https://uk.mathworks.com/help/images/ref/rgb2lab.html.
[18] Song X., Fan G., editors. A study of supervised, semi-supervised and unsupervised multiscale Bayesian image segmentation. The 2002 45th Midwest Symposium on Circuits and Systems, 2002 MWSCAS-2002; 2002: IEEE.
[19] Surlakar P., Araujo S., Sundaram K.M., editors. Comparative Analysis of K-Means and K-Nearest Neighbor Image Segmentation Techniques. 2016 IEEE 6th International Conference on Advanced Computing (IACC); 2016: IEEE.
[20] Cover T., Hart P. Nearest neighbor pattern classification. IEEE transactions on information theory. 1967;13(1):21-27.
[21] Duda R.O., Hart P.E. Pattern classification and scene analysis: Wiley New York; 1973.
[22] Harini R., Chandrasekar C. Image segmentation using nearest neighbor classifiers based on kernel formation for medical images. International Conference on Pattern Recognition, Informatics and Medical Engineering (PRIME-2012): IEEE; 2012. p. 261-265.
[23] MathWorks. Color-Based Segmentation Using the L*a*b* Color Space Natick, MA: The MathWorks; [Date Unknown] [cited 2020 May 13]. Available from: https://uk.mathworks.com/help/images/color-based-segmentation-using-the-l-a-b-color-space.html.
[24] MathWorks. Image Processing Toolbox [Internet]. Natick, MA: The MathWorks; [Date Unknown] [cited 2020 Apr 22]. Available from: https://uk.mathworks.com/products/image.html.
[25] MathWorks. Parallel Computing Toolbox [Internet]. Natick. MA: The MathWorks; [Date Unknown] [cited 2020 Apr 22]. Available from: https://uk.mathworks.com/products/parallel-computing.html.
[26] Hocking R.R. Methods and applications of linear models: regression and the analysis of variance. 3rd ed. Hoboken, NJ: John Wiley & Sons; 2013.